

1 **Title:** Localized anisotropy in the mantle transition zone due to flow through slab
2 gaps

3
4 **Authors:** Han Zhang^{1*}, Brandon Schmandt¹, Jin S. Zhang^{1,2}

5
6 **Affiliations:**

7 1. Department of Earth and Planetary Science, University of New Mexico,
8 Albuquerque, NM, USA.

9 2. Institute of Meteoritics, University of New Mexico, Albuquerque, NM,
10 USA.

11 *Correspondence to: hanzhang@unm.edu

12
13 **Key Points:**

- 14 ● P_{SH}/P_{SV} amplitude ratios between $P660s$ and $P410s$ are useful for
15 constraining transition zone anisotropy
- 16 ● Evidence for up to 2% mantle transition zone anisotropy is found beneath
17 the Pacific Northwest of the U.S.
- 18 ● Mantle flow between slab fragments may enhance development of transition
19 zone anisotropy

20
21 **Abstract:**

22 Measurement of anisotropy advances our understanding of mantle dynamics by
23 linking remote seismic observations to local deformation state through constraints
24 from mineral physics. The Pacific Northwest records the largest depth-integrated
25 anisotropic signals across the western United States but the depths contributing to
26 the total signal are unclear. We used the amplitudes of orthogonally polarized P-to-
27 S converted phases from the mantle transition zone boundaries to identify
28 anisotropy within the ~400-700 km deep layer. Significant anisotropy is found near
29 slab gaps imaged by prior tomography. Focusing of mantle flow through slab gaps
30 may lead to locally elevated stress that enhances lattice preferred orientation of
31 anisotropic minerals within the transition zone, such as wadsleyite.

32
33 **Plain Language Summary:**

34 Earth's mantle convects like a fluid over geological time and it organizes mineral
35 fabrics resulting in directional dependence of seismic velocities, i.e. seismic
36 anisotropy. There is abundant evidence for flow-induced seismic anisotropy at
37 depths above about 400 km, but it is less clear if anisotropy is developed in the
38 mantle transition zone at about 400-700 km deep. Here, we use seismic waves
39 generated from the bottom and top of the transition zone to constrain anisotropy
40 within the layer. Localized evidence of strong anisotropy is found beneath the
41 Pacific Northwest near locations where prior imaging studies show gaps between
42 subducted oceanic plate fragments. We propose that focused flow through
43 constrictions like slab gaps may cause seismic anisotropy in the mantle transition
44 zone.

45

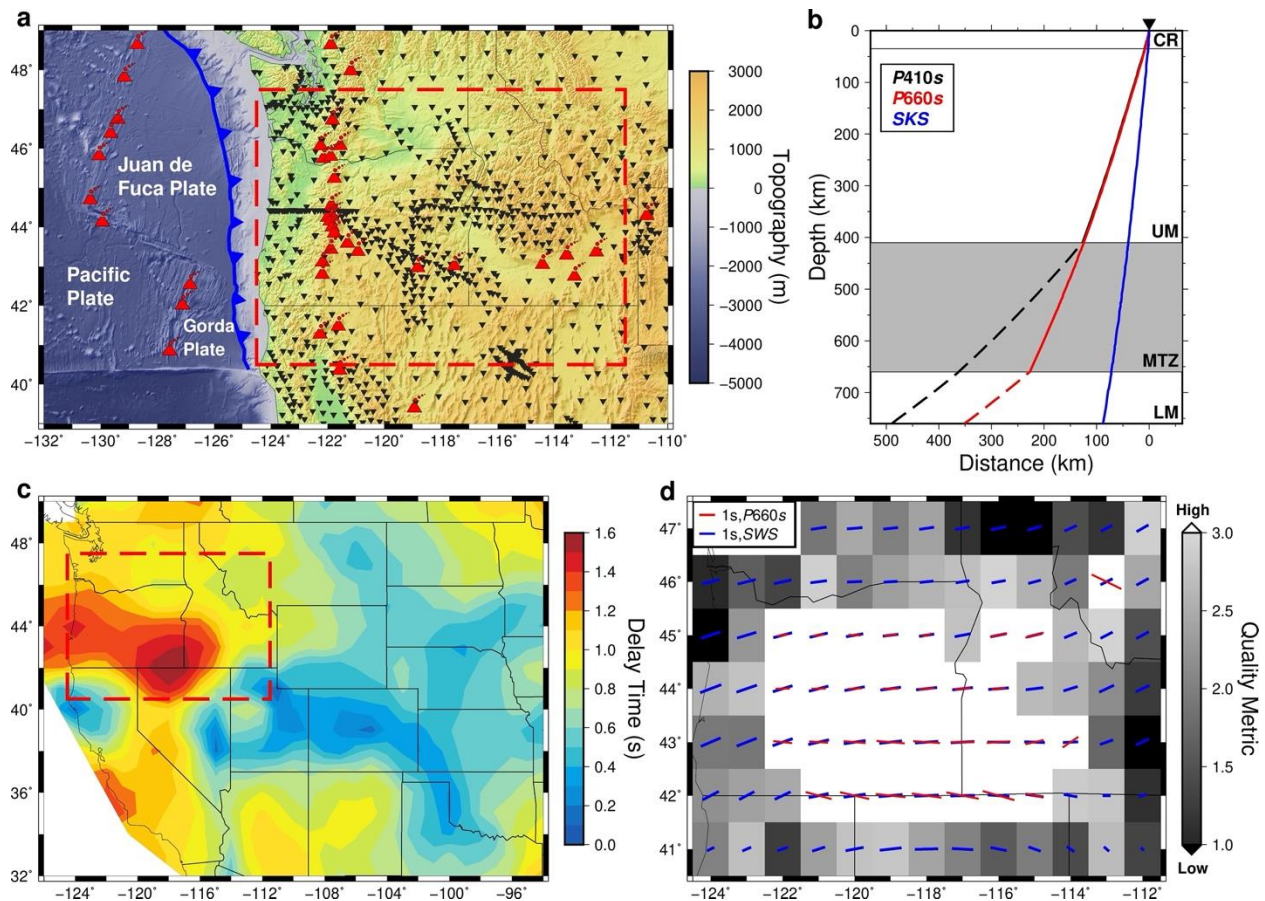
46 **Introduction**

47 Seismic anisotropy of Earth's mantle provides important insights into convective
48 flow and composition at inaccessible depths. There is abundant evidence for
49 concentrated anisotropy at depths within a few hundred kilometers of the mantle's
50 top and bottom, but the prevalence of anisotropy at intermediate depths is more
51 uncertain (Long & Becker, 2010). Potential reasons for diminished anisotropy in
52 the transition zone and most of the lower mantle include decreasing anisotropy of
53 higher-pressure olivine polymorphs (Mainprice 2015; Zhang et al., 2018), strain
54 partitioning into localized shear zones (Girard et al., 2016), and accommodation of
55 strain by diffusion creep rather than dislocation creep (Mohiuddin et al., 2020;
56 Ritterbex et al., 2020). Depth-integrated measurements of mantle anisotropy like
57 teleseismic shear wave splitting (SWS) are often assumed to be dominated by
58 anisotropy at depths less than ~300 km. This perspective is supported by the
59 positive correlation of fast-axis orientations with plate tectonic deformation and
60 surface wave azimuthal anisotropy (Becker et al., 2012; Long & Becker, 2010), as

61 well as isolated evidence that local deep earthquakes exhibit SWS comparable to
62 teleseismic measurements (Fischer & Wiens, 1996). However, some long-
63 wavelength global imaging studies and regional attempts to separate near-source
64 contributions to path-integrated SWS suggest anisotropy extending to mantle
65 transition zone depths of about 400-700 km (Huang et al., 2019; Lynner & Long,
66 2015; Yuan & Beghein, 2013).

67 The Pacific Northwest (PNW) of the U.S. is well-suited to investigate the
68 depth distribution of mantle anisotropy (Fig. 1a). Active subduction is thought to
69 organize vigorous mantle flow, the region has been densely instrumented with
70 broadband seismometers, and a large depth-integrated anisotropy signal is
71 indicated by spatially averaged teleseismic SWS measurements (Liu et al., 2014;
72 Long et al., 2012; Supporting Information S1) (Fig. 1c). Surface wave azimuthal
73 anisotropy constrains regional anisotropy at depths less than about 200 km, but that
74 depth interval can only account for about half of the anisotropy indicated by SWS
75 (Wagner & Long, 2013). Recent attempts using finite-frequency SKS splitting
76 intensity suggest up to 8% anisotropy at 200-400 km to accommodate the
77 remaining signal (Mondal & Long, 2020). However, the amplitude of the
78 sensitivity kernels reduces with depth, leaving uncertainty about anisotropy
79 at >400 km depth. Recent full-waveform inversion (FWI) for anisotropic velocities
80 using regional earthquakes suggests that subduction-driven flow beneath the PNW
81 creates anisotropy at transition zone depths (Zhu et al., 2020). The fast orientations
82 from FWI tomography generally agree with SWS, but the depth-integrated
83 magnitude of anisotropy is much smaller than that obtained by SWS. Thus, it is
84 unclear how much transition zone anisotropy is needed to explain the large depth-
85 integrated SWS signals in the PNW.

86



87
 88 **Fig. 1. Tectonic setting of the PNW and seismic observations of anisotropy.** (a) The Juan de
 89 Fuca Plate is actively subducting beneath the PNW. Holocene volcanoes (red symbols) and
 90 broadband seismometers (black inverse triangles) are superimposed on the topography. The red
 91 dashed box outlines our study area. (b) Ray paths of the $P410s$ (black), $P660s$ (red) and SKS
 92 (blue) phases. Compositional layers are labeled: crust (CR), upper mantle (UM), mantle
 93 transition zone (MTZ), and lower mantle (LM). (c) Spatially averaged SWS delay times in the
 94 western U.S. The red dashed box outlines our study region. (d) Comparison between our
 95 estimated splitting parameters from the $P660s$ (red bar) and the spatially averaged SWS results
 96 (blue bar). The grayscale background indicates the quality of the estimations from the $P660s$.

97

98 Data and Method

99 This study takes advantage of teleseismic P-to-S (P_s) conversions at the boundaries
 100 of the mantle transition zone to isolate potential deep contributions to anisotropy
 101 beneath the PNW. The two converted phases, $P410s$ and $P660s$, almost share ray
 102 paths in the upper mantle so the paired observations can localize signals from
 103 within the transition zone (Fig. 1b). In an isotropic mantle with 1-D velocity

104 structure, *Ps* conversions would only be observed with P-SV polarization. But
105 constructive anisotropy along the shear wave ray path can cause splitting effect,
106 leading to observations of *Ps* energy on SH polarization. We collected broadband
107 waveform data from teleseismic earthquakes with magnitude greater than 5.5. For
108 data with P wave signal-to-noise ratio (SNR) greater than 3, we extracted 3-
109 component (P-SV-SH) receiver functions using a multimode frequency domain
110 deconvolution method (Mercier et al., 2006). The receiver functions were filtered
111 using a zero-phase bandpass filter between 0.07 Hz and 0.25 Hz and corrected for
112 normal moveout by extracting velocities along the ray paths within a previous
113 tomographic model (Schmandt & Lin, 2014).

114 Since small delay times often yield undetectable *Ps* signal on the SH
115 component (Montagner et al., 2000), stacking many waveforms is often required
116 and attempts to use the two phases are limited to areas with strong anisotropy
117 (Vinnik & Montagner, 1996; Kong et al., 2018). Based on their piercing points at
118 500 km depth, we stacked the receiver functions that sample the transition zone in
119 200 km radius caps. We then applied a bootstrap based quality metric to determine
120 regions with adequate SNR to constrain transition zone anisotropy (Fig. 1d;
121 Supporting Information S2). The region with adequate *P660s* signals corresponds
122 well with the area of large SWS delay times (>1.3 s, Fig. 1c). The splitting
123 parameters, fast-axis orientation and delay time, estimated from *P660s* using
124 transverse energy minimization (Long & Silver, 2009; Walsh et al., 2013) also
125 share great similarity with the SWS results, indicating that most of the anisotropic
126 signals can be explained at depths above the 660 (Fig. 1d). The mean difference of
127 the fast-axis orientation estimates is 6.1° with a standard deviation of 11.8° , and the
128 mean difference of delay times is -0.03 s with a standard deviation of 0.34 s.
129 However, the transverse component energy minimization approach to measuring
130 anisotropy results in large delay time uncertainties (~ 0.5 s) for the *P410s* and

131 *P660s* estimations at individual stacking points, so they are not optimal for
132 constraining the potentially weak anisotropy in the transition zone.

133 The amplitude ratio of the conversions between the two shear wave
134 components (P_{SH}/P_{SV}) provides greater sensitivity to the magnitude of anisotropy
135 than the delay time (Fig. S1). Consequently, the differences in the P_{SH}/P_{SV}
136 amplitude ratios between *P660s* and *P410s* reflect transition zone anisotropy more
137 precisely. Pairing the two *Ps* phases during the measurement further eliminates the
138 back-azimuth component from the anisotropic effects. We again measured the
139 amplitude ratios using stacks in 200 km radius caps and applied bootstrap
140 resampling to assess the uncertainty (Supporting Information S3). The
141 measurement of amplitude ratios of receiver functions is similar to the
142 conventional method of measuring splitting intensity for the *SKS* phase (Chevrot,
143 2000). The splitting intensity is defined as the amplitude ratio of the *SKS* phase
144 between the transverse component and the time derivative of the radial component.
145 In contrast, we measured the amplitude ratio of the stacked *Ps* phase between the
146 time integrated SH component (P_{SH}) and original SV component (P_{SV}).
147 Mathematically, the derivative and integration processes offer identical results
148 after removing the integration constant. The integration process we adopted here
149 preserves the one-side polarity of the P_{SV} phase, which simplifies the
150 measurements (Fig. S1).

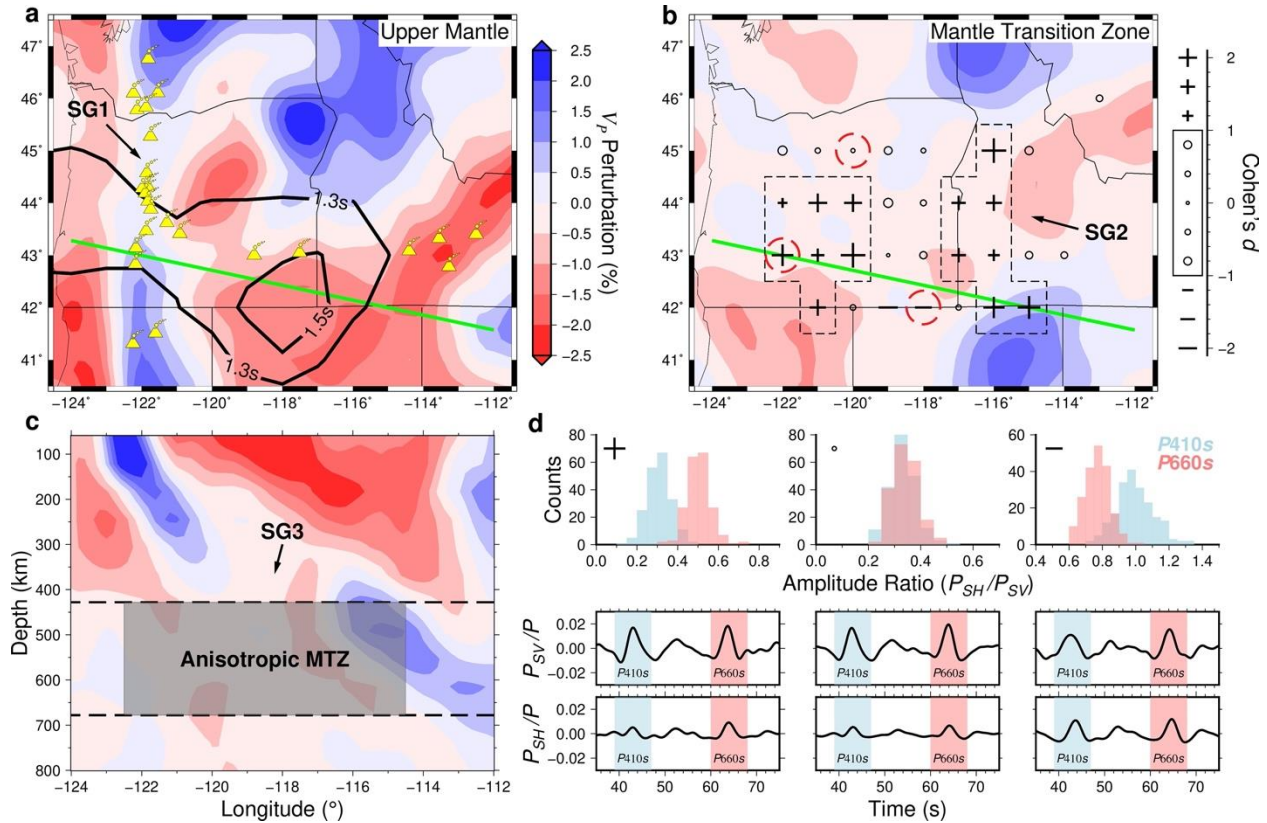
151

152 **Results and Discussion**

153 The null hypothesis of an isotropic transition zone and all anisotropy above the 410
154 predicts indistinguishable amplitude ratio distributions for the two phases. We use
155 Cohen's distance between the *P660s* and *P410s* amplitude ratio distributions and
156 the corresponding paired t-test to evaluate the significance of transition zone
157 anisotropy (Supporting Information S3). About half of the resulting Cohen's

158 distances show a significant difference at 68% confidence (± 1.0), with a few
 159 locations exceeding the 95% confidence level (± 2.0) (Fig. 2, b and d, See Fig. S2
 160 for more examples).

161



162

163 **Fig. 2. Seismic tomography of the study region and amplitude ratio evidence for**
 164 **anisotropy.** Depth averaged V_p perturbation within (a) the upper mantle (60-350 km) and (b) the
 165 mantle transition zone (435-635 km). The positions of slab gaps are labeled by SG. Holocene
 166 volcanoes (yellow symbols), contoured spatially averaged SWS delay times (1.3s and 1.5s, black
 167 lines), and observed Cohen's distances are superimposed on the tomography. (c) Cross section of
 168 the V_p perturbation beneath the green line on the maps. The gray box outlines where mantle
 169 transition zone (MTZ) anisotropy is required by the observations. (d) Examples of the observed
 170 amplitude ratios and stacked waveforms from the locations with red dashed circles in panel b.
 171 The amplitude ratios from the P_{410s} are in red while those from P_{660s} are in blue.

172

173 We defined three categories for the observed results: constructive
 174 interference where P_{660s} amplitude ratios are greater than P_{410s} amplitude ratios
 175 (labeled '+'), destructive interference where P_{410s} amplitude ratios are greater

176 than those of $P660s$ (labeled ‘-’), and neutral where there is no significant
177 difference (labeled ‘o’; Fig. 2b). The neutral observations fail to reject the null
178 hypothesis of an isotropic transition zone. Two larger areas of constructive
179 interference and one smaller area of destructive interference indicate localized
180 transition zone anisotropy inboard of the Cascades volcanic arc (Fig. 2c).

181 The two constructive interference areas exhibit greater path-integrated
182 anisotropy from the 660 to the surface compared to that from the 410 to the
183 surface. Such observations can be fit with a common fast orientation for an
184 anisotropic layer extending through the upper mantle and into the transition zone.
185 Both constructive interference areas lie within gaps between high-velocity slab
186 fragments identified by seismic tomography (Schmandt & Lin, 2014; Hawley &
187 Allen, 2019) (Fig. 2, a and b, labeled SG; see Movie S1 for 3D illustration). The
188 western area is located near an along-strike slab gap in the upper mantle beneath
189 the central to southern Oregon backarc region that is hypothesized to focus mantle
190 flow beneath backarc volcanic provinces (Hawley & Allen, 2019). The eastern area
191 of constructive interference is located between two high-velocity features
192 interpreted to be older slab fragments located further beneath the continental
193 interior (Liu & Stegman, 2011; Schmandt & Humphreys, 2011). The southern edge
194 of the eastern constructive interference area appears to overlap the position of the
195 high-velocity slab beneath northern Nevada.

196 Two stacking points that exhibit destructive interference of transition zone
197 and upper mantle anisotropy are located at the southern edge of the well-resolved
198 area (Fig. 2b). Destructive interference of splitting within the transition zone
199 and above it due to changing fast orientation with depth can create a larger P_{SH}/P_{SV}
200 amplitude ratio of the $P410s$ compared to that of $P660s$ (Fig. S3; Supporting
201 Information S4). Given the small area that exhibits destructive interference and the
202 tradeoffs among estimating the thickness, fast orientation, and magnitude of

203 anisotropy for the two layers, we refrain from further interpretation of these two
204 stacking points.

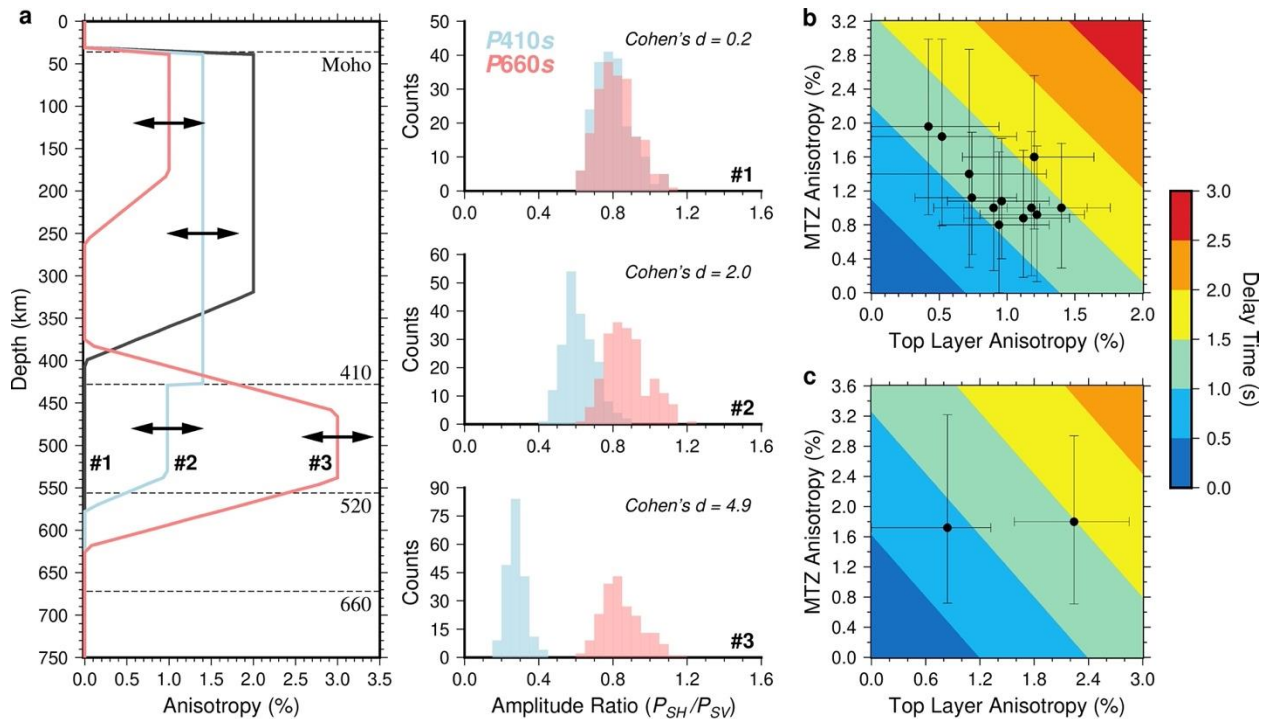
205 Anisotropy within the transition zone could arise on account of lattice
206 preferred orientation (LPO) of olivine polymorphs. Wadsleyite is the stable
207 polymorph of olivine in the upper transition zone and has a maximum single-
208 crystal shear wave anisotropy of ~9% (Zhang et al., 2018). The peak anisotropy is
209 smaller than that of olivine above the 410 (Fig. S4), but deformation experiments
210 have successfully produced up to 2% anisotropy of wadsleyite (Kawazoe et al.,
211 2013; Ohuchi et al., 2014). At lower transition zone depths, the stable polymorph
212 of olivine is ringwoodite and it is elastically almost isotropic at transition zone
213 pressures (Mainprice, 2015). Therefore, it is unlikely to contribute to the observed
214 anisotropic signals. Atypical anisotropic minerals formed near or within the
215 subducted slab may contribute to anisotropy. At relatively low mantle
216 temperatures, two strongly anisotropic minerals, phase E and akimotoite, could
217 form at transition zone depths (Hao et al., 2019; Satta et al., 2019). Phase E is a
218 reaction product between olivine and water at upper transition zone depths (Satta et
219 al., 2019). Akimotoite is enriched in the refractory harzburgitic lithosphere of the
220 slabs at lower transition zone depths (Ishii et al., 2019). Both minerals have single-
221 crystal shear wave anisotropy up to ~20%, which makes them alternative
222 candidates for the origin of observed anisotropic signals in the transition zone.

223 The deformation mechanisms for the mantle transition zone minerals depend
224 on many factors, such as temperature, flow stress, strain rates, and grain size. The
225 laboratory determined glide-driven dislocation creep of transition zone minerals can
226 cause development of LPO (Kawazoe et al., 2013). However, a recent theoretical
227 study suggests that deformation in the mantle transition zone is dominated by
228 climb-driven dislocation creep, which does not develop LPO (Ritterbex et al.,
229 2020). The glide-driven dislocation creep is favored by high stress and strain rates in

230 the laboratory, whereas typical flow stress and strain rates in the ambient mantle
 231 are several orders lower. Therefore, the development of LPO may be expected only
 232 in areas of stress concentration, such as where mantle flow is focused through
 233 constrictions (Alisic et al., 2012; Király et al., 2020).

234 Based on the mineral physics' constraints, we constructed three types of
 235 forward models to illustrate a range of potential anisotropic structures (Fig. 3a;
 236 Supporting Information S5). The simplest model includes only upper mantle
 237 anisotropy extending from the Moho to 400 km depth, such that anisotropy is
 238 consistent with only an olivine LPO origin (Fig. 3a, #1). Since there is no
 239 anisotropy within the transition zone, the first model can explain the neutral
 240 observations where the P_{SH}/P_{SV} amplitude ratios from the P660s and P410s are
 241 indistinguishable.

242



243

244 **Fig. 3. Forward models and the inverted mantle transition zone anisotropy.** (a) Three types
 245 of forward models (#1-3) and their corresponding amplitude ratios distributions. The Cohen's
 246 distances are denoted by the histograms. (b) Inverted mantle transition zone (MTZ) anisotropy
 247 for most of the constructive interference areas using parameterization of model #2. The error bar

248 represents the 68% confidence intervals. The color background represents the delay time from a
249 vertically propagated shear wave. (c) Inverted results for the two stacking points in the
250 southeastern corner using parameterization of model #3.

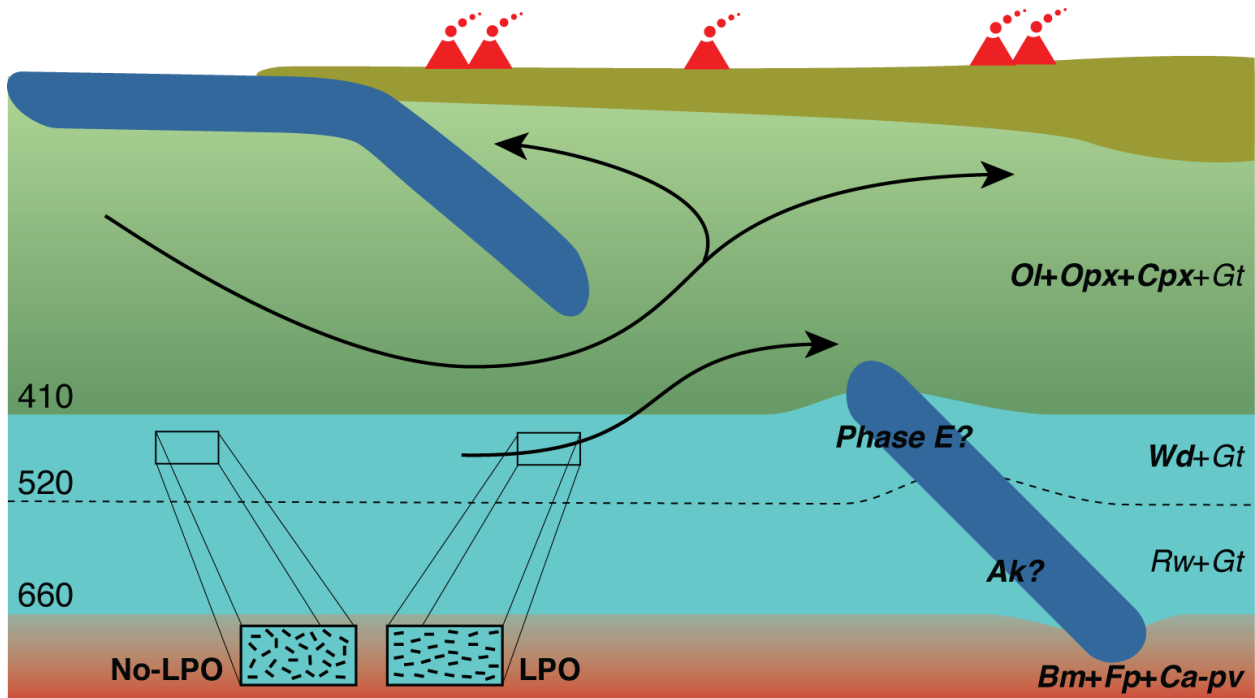
251
252 The second model also contains upper mantle anisotropy, but it is underlain
253 by an anisotropic layer in the upper part of the transition zone where wadsleyite is
254 stable (Fig. 3a, #2). This model yields constructive interference of transition zone
255 and upper mantle splitting effect and then offers a plausible explanation for places
256 with a larger $P660s$ amplitude ratio. With this model parameterization, we used a
257 grid search of upper mantle and transition zone anisotropy magnitudes to find the
258 best model for explaining the observations (Supporting Information S6). Using a
259 ray parameter and back-azimuth distribution identical to the observational data, the
260 inverted results show that inclusion of $\sim 1-2\%$ anisotropy in the upper mantle
261 transition zone can reproduce the observed differences between the two amplitude
262 ratios for most stacking points exhibiting constructive interference (Fig. 3b).

263 The third model is built on the idea that subducted slab is present in the
264 transition zone, thus atypical minerals which are not expected in the ambient
265 mantle may contribute to anisotropy (Fig. 3a, #3). In this case, the anisotropy
266 within the transition zone is allowed to extend to deeper depths where wadsleyite is
267 no longer stable. The deeper anisotropy may arise from akimotoite associated with
268 the cool slab fragment, such as beneath the southeastern corner of the well-
269 resolved area (Fig. 2b). When modeling the two stacking points in the southeastern
270 corner, the additional thickness of the anisotropic layer prevents requiring
271 unreasonably large anisotropy in the wadsleyite stability field (Fig. 3c).

272 The three anisotropic structures suggest various geodynamic settings (Fig.
273 4). The first model represents upper mantle flow due to absolute plate motion and
274 subduction zone corner flow in the shallow upper mantle. In this conventional
275 context, anisotropy is primarily due to olivine LPO created by flow-induced

276 dislocation creep. The second model requires focused mantle flow caused by slab
 277 ruptures as hypothesized by prior geodynamic modeling of regional mantle flow
 278 and anisotropic fast orientations (Zhou et al., 2018). If flow through slab gaps
 279 induces locally high stress at transition zone depths, the LPO of wadsleyite could
 280 contribute a portion (up to 0.4 s in this study) of the total splitting delay time. The
 281 additional anisotropy at transition zone depths helps explain the large discrepancy
 282 between estimated splitting delay times from surface wave azimuthal anisotropy
 283 studies and observed teleseismic SWS in the central Cascades backarc (Wagner &
 284 Long, 2013). The third model represents the potential influence of compositional
 285 heterogeneity due to a slab fragment at transition zone depths, which is a scenario
 286 that may be even more important for subduction zones with older and colder slab
 287 fragments in the transition zone.

288



289

290 **Fig. 4. Schematic model of flow going through slab gap.** The rupture of a continuous slab
 291 induces enhanced flow near the slab gap. The resulting flow concentrates stress and develops
 292 lattice preferred orientation (LPO) of anisotropic minerals at transition zone depths. Common
 293 minerals are labeled using italic font with anisotropic minerals in bold: olivine (Ol),

294 orthopyroxene (Opx), clinopyroxene (Cpx), garnet (Gt), wadsleyite (Wd), ringwoodite (Rw),
295 bridgmanite (Bm), ferropericlasite (Fp), Ca-perovskite (Ca-pv), akimotoite (Ak).

296

297 **Conclusions**

298 The new results support the potential development of seismic anisotropy at mantle
299 transition zone depths, with magnitudes that can be similar to those in the upper
300 mantle. However, in contrast to upper mantle anisotropy that is observed
301 ubiquitously, it appears that transition zone anisotropy may be restricted to areas of
302 locally high stress such as focused flow through fragmented slabs.

303

304 **References**

- 305 1. Alisic, L., Gurnis, M., Stadler, G., Burstedde, C., & Ghattas, O. (2012). Multi-scale dynamics
306 and rheology of mantle flow with plates. *Journal of Geophysical Research: Solid*
307 *Earth*, 117(B10).
- 308 2. Becker, T. W., Lebedev, S., & Long, M. D. (2012). On the relationship between azimuthal
309 anisotropy from shear wave splitting and surface wave tomography. *Journal of Geophysical*
310 *Research: Solid Earth*, 117(B1).
- 311 3. Chevrot, S. (2000). Multichannel analysis of shear wave splitting. *Journal of Geophysical*
312 *Research: Solid Earth*, 105(B9), 21579-21590.
- 313 4. Fischer, K. M., & Wiens, D. A. (1996). The depth distribution of mantle anisotropy beneath
314 the Tonga subduction zone. *Earth and Planetary Science Letters*, 142(1-2), 253-260.
- 315 5. Girard, J., Amulele, G., Farla, R., Mohiuddin, A., & Karato, S. I. (2016). Shear deformation
316 of bridgmanite and magnesiowüstite aggregates at lower mantle conditions. *Science*,
317 351(6269), 144-147.
- 318 6. Hao, S., Wang, W., Qian, W., & Wu, Z. (2019). Elasticity of akimotoite under the mantle
319 conditions: Implications for multiple discontinuities and seismic anisotropies at the depth
320 of~ 600–750 km in subduction zones. *Earth and Planetary Science Letters*, 528, 115830.
- 321 7. Hawley, W. B., & Allen, R. M. (2019). The fragmented death of the Farallon plate.
322 *Geophysical Research Letters*, 46(13), 7386-7394.
- 323 8. Huang, Q., Schmerr, N., Waszek, L., & Beghein, C. (2019). Constraints on seismic
324 anisotropy in the mantle transition zone from long-period SS precursors. *Journal of*
325 *Geophysical Research: Solid Earth*, 124(7), 6779-6800.
- 326 9. Ishii, T., Kojitani, H., & Akaogi, M. (2019). Phase Relations of Harzburgite and MORB up
327 to the Uppermost Lower Mantle Conditions: Precise Comparison With Pyrolite by
328 Multisample Cell High-Pressure Experiments With Implication to Dynamics of Subducted
329 Slabs. *Journal of Geophysical Research: Solid Earth*, 124(4), 3491-3507.

- 330 10. Kawazoe, T., Ohuchi, T., Nishihara, Y., Nishiyama, N., Fujino, K., & Irifune, T. (2013).
331 Seismic anisotropy in the mantle transition zone induced by shear deformation of wadsleyite.
332 *Physics of the Earth and Planetary Interiors*, 216, 91-98.
- 333 11. Király, Á., Portner, D. E., Haynie, K. L., Chilson-Parks, B. H., Ghosh, T., Jadamec, M., et
334 al., (2020). The effect of slab gaps on subduction dynamics and mantle
335 upwelling. *Tectonophysics*, 785, 228458.
- 336 12. Kong, F., Gao, S.S., Liu, K.H., Song, J., Ding, W., Fang, Y., Ruan, A., & Li, J. (2018).
337 Receiver function investigations of seismic anisotropy layering beneath Southern California.
338 *Journal of Geophysical Research: Solid Earth*, 123(12), 10-672.
- 339 13. Liu, L., & Stegman, D. R. (2011). Segmentation of the Farallon slab. *Earth and Planetary
340 Science Letters*, 311(1-2), 1-10.
- 341 14. Liu, K.H., Els Sheikh, A., Lemnifi, A., Purevsuren, U., Ray, M., Refayee, H., et al., (2014). A
342 uniform database of teleseismic shear wave splitting measurements for the western and
343 central United States. *Geochemistry, Geophysics, Geosystems*, 15(5), 2075-2085.
- 344 15. Long, M. D., Becker, T. W. (2010). Mantle dynamics and seismic anisotropy. *Earth and
345 Planetary Science Letters*, 297(3-4), 341-354.
- 346 16. Long, M. D., & Silver, P. G. (2009). Shear wave splitting and mantle anisotropy:
347 Measurements, interpretations, and new directions. *Surveys in Geophysics*, 30(4), 407-461.
- 348 17. Long, M.D., Till, C.B., Druken, K.A., Carlson, R.W., Wagner, L.S., Fouch, M.J., et al.,
349 (2012). Mantle dynamics beneath the Pacific Northwest and the generation of voluminous
350 back-arc volcanism. *Geochemistry, Geophysics, Geosystems*, 13(8).
- 351 18. Lynner, C., & Long, M. D. (2015). Heterogeneous seismic anisotropy in the transition zone
352 and uppermost lower mantle: evidence from South America, Izu-Bonin and Japan.
353 *Geophysical Journal International*, 201(3), 1545-1552.
- 354 19. Mainprice, D. (2015) Seismic anisotropy of the deep Earth from a mineral and rock physics
355 perspective. *Treatise in Geophysics*, 2nd Edition, Volume 2, 487-538
- 356 20. Mercier, J. P., Bostock, M. G., & Baig, A. M. (2006). Improved Green's functions for
357 passive-source structural studies. *Geophysics*, 71(4), SI95-SI102.
- 358 21. Mohiuddin, A., Karato, S. I., & Girard, J. (2020). Slab weakening during the olivine to
359 ringwoodite transition in the mantle. *Nature Geoscience*, 13(2), 170-174.
- 360 22. Mondal, P., & Long, M. D. (2020). Strong seismic anisotropy in the deep upper mantle
361 beneath the Cascadia backarc: Constraints from probabilistic finite-frequency SKS splitting
362 intensity tomography. *Earth and Planetary Science Letters*, 539, 116172.
- 363 23. Montagner, J. P., Griot-Pommer, D. A., & Lavé, J. (2000). How to relate body wave and
364 surface wave anisotropy?. *Journal of Geophysical Research: Solid Earth*, 105(B8), 19015-
365 19027.
- 366 24. Ohuchi, T., Fujino, K., Kawazoe, T., & Irifune, T. (2014). Crystallographic preferred
367 orientation of wadsleyite and ringwoodite: Effects of phase transformation and water on
368 seismic anisotropy in the mantle transition zone. *Earth and Planetary Science Letters*, 397,
369 133-144.

- 370 25. Ritterbex, S., Carrez, P., & Cordier, P. (2020). Deformation across the mantle transition
371 zone: A theoretical mineral physics view. *Earth and Planetary Science Letters*, 547, 116438.
- 372 26. Satta, N., Marquardt, H., Kurnosov, A., Buchen, J., Kawazoe, T., McCammon, C., &
373 Ballaran, T. B. (2019). Single-crystal elasticity of iron-bearing phase E and seismic detection
374 of water in Earth's upper mantle. *American Mineralogist*, 104(10), 1526-1529.
- 375 27. Schmandt, B., & Humphreys, E. (2011). Seismically imaged relict slab from the 55 Ma
376 Siletzia accretion to the northwest United States. *Geology*, 39(2), 175-178.
- 377 28. Schmandt, B., & Lin, F. C. (2014). P and S wave tomography of the mantle beneath the
378 United States. *Geophysical Research Letters*, 41(18), 6342-6349.
- 379 29. Vinnik, L., & Montagner, J. P. (1996). Shear wave splitting in the mantle Ps phases.
380 *Geophysical Research Letters*, 23(18), 2449-2452.
- 381 30. Wagner, L. S., & Long, M. D. (2013). Distinctive upper mantle anisotropy beneath the High
382 Lava Plains and Eastern Snake River Plain, Pacific Northwest, USA. *Geochemistry,*
383 *Geophysics, Geosystems*, 14(10), 4647-4666
- 384 31. Walsh, E., Arnold, R., & Savage, M. K. (2013). Silver and Chan revisited. *Journal of*
385 *Geophysical Research: Solid Earth*, 118(10), 5500-5515.
- 386 32. Yuan, K., & Beghein, C. (2013). Seismic anisotropy changes across upper mantle phase
387 transitions. *Earth and Planetary Science Letters*, 374, 132-144
- 388 33. Zhang, J. S., Bass, J. D., & Schmandt, B. (2018). The elastic anisotropy change near the 410-
389 km discontinuity: Predictions from single-crystal elasticity measurements of olivine and
390 wadsleyite. *Journal of Geophysical Research: Solid Earth*, 123(4), 2674-2684.
- 391 34. Zhou, Q., Hu, J., Liu, L., Chaparro, T., Stegman, D. R., & Faccenda, M. (2018). Western US
392 seismic anisotropy revealing complex mantle dynamics. *Earth and Planetary Science Letters*,
393 500, 156-167.
- 394 35. Zhu, H., Li, X., Yang, J., Stern, R. J., & Lumley, D. E. Poloidal-and toroidal-mode mantle
395 flows underneath the Cascadia Subduction Zone. *Geophysical Research Letters*,
396 e2020GL087530.

397

398 **References only in the supporting information**

- 399 36. Levin, V., & Park, J. (1997). Crustal anisotropy in the Ural Mountains foredeep from
400 teleseismic receiver functions. *Geophysical Research Letters*, 24(11), 1283-1286.
- 401 37. Zhang, H., & Schmandt, B. (2019). Application of Ps scattering kernels to imaging the
402 mantle transition zone with receiver functions. *Journal of Geophysical Research: Solid*
403 *Earth*, 124(1), 709-728.

404

405 **Acknowledgments:**

406 We thank K. H. Liu and S. S. Gao for sharing their SWS dataset. We also thank H.
407 Zhu for sharing full waveform inversion results. This study is supported by NSF

408 grants EAR-1554908 and EAR-1664471. H.Z. acknowledges support from the
409 Caswell Silver Fellowship of the Earth and Planetary Science Department at the
410 University of New Mexico.

411

412 **Data Availability**

413 The raw seismic data used in this study are publicly available through the IRIS
414 Data Management Center. The receiver functions data are available at Zenodo
415 (<https://doi.org/10.5281/zenodo.3981446>).

416